Egypt. J. Chem. **Vol.** 64, No. 10 pp. 5627- 5645 (2021)

Egyptian Journal of Chemistry

http://ejchem.journals.ekb.eg/

Synthesis and Characterization of Magnetic Nickel Ferrite-Modified Montmorillonite Nanocomposite for Cu (II) and Zn (II) Ions Removal from Wastewater

Hanan A. Ahmed [a,*], Mona S. S. Soliman [b], Sahar A. Othman [b]

[a] *Petrochemicals Department, Egyptian Petroleum Research Institute, Nasr City, Cairo, 11765, Egypt*

[b] *Central Laboratory for Environmental Quality Monitoring, National Water Research Center, El-Kanater, 13621/6, Egypt*

Abstract

For the adsorption of copper (II) and zinc (II) ions from polluted water, an efficient inexpensive nanoadsorbent; nickel ferrite-modified montmorillonite nanocomposite was synthesized by co-precipitation of the mechano-chemically modified montmorillonite with the salts of nickel and iron. The natural MMT, modified MMT, and the synthesized nickel ferrite-modified montmorillonite ($NiFe_2O_4$-Mod MMT) nanoadsorbent were characterized by several techniques including Fourier transform infrared spectroscopy, X-ray diffraction, transmission electron microscopy, energy-dispersive X-ray, surface area analysis, saturation magnetization, and surface zeta potential. Batch studies were carried out on the effect of various parameters including contact time, nanocomposite dosage, solution pH, metal ion initial concentration, and temperature on the adsorption process to optimize its conditions. The equilibrium state was reached after 60 min and 90 min of reaction for Cu (II) and Zn (II) ions, respectively. The optimum conditions were 0.1 g adsorbent dose, pH 5, 13 mg/L initial metal ion concentration and 298 K temperature for copper (II) adsorption and 0.1 g adsorbent dose, pH 6, 6 mg/L initial metal ion concentration, and 298 K temperature for zinc (II) adsorption. Among the designed kinetic and equilibrium models, the pseudo-second-order kinetic model and Langmuir adsorption isotherm model have controlled the adsorption process for both metal ions. Furthermore, the adsorption mechanism and the reproducibility of the nanoadsorbent were investigated. The maximum adsorption efficiency was 99.23% and 91.67% of copper (II) and zinc (II) ions, respectively.

Keywords: Synthesis; Characterization; Adsorption; Heavy metals; Magnetic nanocomposite; Adsorption Kinetic; Isotherm

1. Introduction

One of the most toxic substances to the environment is heavy metals. Wastewater full of heavy metals originates mainly from mining operations, metal plating equipment, fertilizer industries, tanneries, batteries, paper & pesticide manufactories, thermoplastics, and pigment manufacture, etc. [1]. These industries get rid of their wastewater, full of heavy metals, in direct or indirect ways to the environment. Heavy metals appear to accumulate in living organisms, because of their toxicity and non-biodegradability. So they can cause a lot of acute and chronic diseases. The treatment of industrial wastewater, including heavy metals, is becoming an important subject for improving water quality. Copper (II) is considered one of the most toxic metals for living organisms when its concentration exceeds the required limits. Its extensive intake can cause kidney retention and liver function disruption, and also it affects badly on the nervous and reproductive systems or even can lead to death [2]. However, the undue intake of zinc (II) (as a toxic metal) can result in acute gastrointestinal, cholesterol metabolism, and brain, heart, or kidney damage [3]. Several methods of wastewater treatment like chemical precipitation, coagulation, and membrane processes can be utilized to eliminate heavy metals. Such processes are mostly either expensive or do not decrease the limits of heavy metals to the required one [4]. Adsorption is a

*Corresponding author e-mail: drhananepri@yahoo.com
Receive Date: 26 March 2021, Revise Date: 24 May 2021, Accept Date: 01 June 2021
DOI: 10.21608/EJCHEM.2021.69597.3527

preferred technique for pollutants removal from water because of its excellent properties like low cost, abundant sources of adsorbent, high efficiency, and easy handling [5]. Though the mentioned advantages of the adsorption process, many efforts are still needed to find a way to isolate pollutants and adsorbents from the treated water by selecting a suitable adsorbent [5]. Many adsorbents like chitosan, activated carbon, natural zeolite, clays, and industrial and agricultural wastes were used to adsorb heavy metal ions of various types [5]. Montmorillonite (MMT) clay has two tetrahedral sheets of silica sandwiching a central octahedral sheet of alumina (T-O-T) [6] and owing to the isomorphic ionic substitutions in the T–O–T structure [7]; its surface has net structural negative charge making it able to adsorb various positively charged species [8]. Because of the green nature, low-cost, non-toxicity, availability, mechanical stability, layered structure, and high cation exchange capacity of clays like MMT, they are utilized as attractive adsorbents for different pollutants elimination [9]. Thorough investigating the outcomes of these studies it showed that the removal capacity of clays is high, however; their mechanical activation via ball milling was reported in the literature [10]. Utilization of this green chemistry technique i.e. ball milling, for clay modification can be resulted in various structural transformations, chemical reactions, particle size reduction, and may cause the mechanical activation of the treated clay which can enhance their adsorption capacity avoiding high calcination temperatures [11]. It also has the advantages of small energy requirements, low processing temperatures thereby reduced costs, and increased environmental friendliness [12]. Magnetic composites may be considered as alternative adsorbents to achieve this target due to their unique adsorption activity and magnetic properties, which make them separated easily by applying an external magnetic field. Nickel ferrite is one of the most flexible ferrite (magnetic) materials because of its fascinating properties which make it an effective adsorbent and applied in various applications [13-15]. Among the different chemical techniques used for the $NiFe_2O_4$ nano-particles preparation co-precipitation method is widely utilized based on the ease and reproducibility [16].

Based on the mentioned above concerns, the primary purpose of this research was to mechanically-chemically (mechanochemically) modify the naturally available montmorillonite (MMT) clay and used it as a support to synthesize a new eco-friendly and efficient cost-effective magnetic nanoadsorbent; nickel ferrite-modified montmorillonite $NiFe_2O_4$-modified montmorillonite ($NiFe_2O_4$-Mod MMT) nanocomposite. Secondly, the natural MMT (MMT), modified MMT (Mod MMT), and the synthesized nickel ferrite-modified montmorillonite ($NiFe_2O_4$-Mod MMT) nanocomposite characteristics were elucidated by several techniques including Fourier transform infrared (FTIR) spectroscopy, X-ray diffraction (XRD), transmission electron microscopy (TEM), energy-dispersive X-ray (EDX), surface area analysis, saturation magnetization (VSM), and surface zeta potential. Thirdly, the synthesized nanoadsorbent was applied for the elimination of Cu (II) and Zn (II) ions from polluted water to minimize the high-cost issue of industrial wastewater treatment in most developing countries. Five factors affecting the adsorption process including contact time, $NiFe_2O_4$-Mod MMT composite dosage, metal ion initial concentration, solution pH, and temperature were explored. Fourthly, nonlinear regression was designed for various kinetic and equilibrium models to evaluate the adsorption data. Finally, the adsorption mechanism and the reproducibility of the nanoadsorbent were also investigated.

2. Materials and methods

2.1. Reagents and materials

Deionized water was used for preparing all solutions. The reagents and chemicals in the experimental study were purchased and used without further purification. $Fe(NO_3)_3.9H_2O$, $Ni(NO_3)_2.6H_2O$, $Cu(NO_3)_2.3H_2O$, and $Zn(NO_3)_2.6H_2O$ were purchased from Sigma–Aldrich. (NaOH, 98%) and (HCl, 37%) were analytical grades, obtained from Merck Chemical Co. Natural montmorillonite clay was collected from El Nakheel area, western desert, Egypt, ball-milled, and used after purification.

2.2. Mechanochemical modification of montmorillonite clay

Egyptian raw montmorillonite (MMT) clay was ball milled; mechanomodified, as previously reported by Yan et al 2015 [17] with some changes. Specifically, (MMT) was dried at 110 °C until a constant weight was obtained. Then, a definite amount of (MMT) was milled at 300 rpm for 300 min (FRITSCH (Pulverisette) Ball Mill, Zirconium-Oxide Balls) in 500 mL zirconium oxide vessel at 50 Hz.

The resulting sample was purified by removing the organic matter impurities by treating it with hydrogen peroxide (p.a. 30%) and a definite amount of distilled water under stirring at 550 rpm for 3 h at 70 °C. After that, the precipitate was washed with deionized water several times and centrifuged at 1500 rpm for 5 min. The resulting sample was treated with 5% HCl acid

solution under stirring at 550 rpm for 3 h at 70 °C to activate it. Afterward, the suspension was centrifuged at 3000 rpm for 5 min and the isolated clay was washed repeatedly by deionized water to remove the residual Cl^{-1} ions. The precipitate was finally muffling calcined in air at 400 °C for 2 h, labelled as (Mod MMT), and stored for further analysis and studies.

2.3. Synthesis of nickel ferrite-modified montmorillonite nanocomposite

Nickel ferrite-modified montmorillonite **(**$NiFe_2O_4$-Mod MMT) magnetic nanocomposite was synthesized in one pot by co-precipitation of (Mod MMT) with the salts of nickel and iron. Aqueous solutions of $Ni(NO_3)_2{\cdot}6H_2O$ and $Fe(NO_3)_3{\cdot}9H_2O$ with a molar ratio of (1: 2) respectively were mixed under stirring about 30 min to get a homogeneous mixture solution. Then the above mixture is added to a certain amount (2.25 g) of (Mod MMT) dispersed in distilled water and stirring them under 350 rpm at 40 °C for 1 h; where the molar ratio of $NiFe_2O_4$: Mod MMT clay was 1:1 from the total weight of the composite. Sodium hydroxide solution (1 mol/L) was slowly added to the mixed solution with stirring at 550 rpm and the temperature was held at 40 °C till the formation of composite beads, and the stirring was continued for a further 1 h. Then, the solution was left to stabilize. The precipitate was separated magnetically and washed by warm distilled water many times for the elimination of Na^+ ions. The final nanocomposite was obtained after drying the precipitate at 105 °C for 4 h.

2.4. Characterization

2.4.1. Fourier transform infrared (FTIR) spectra

FTIR analysis was done by the Nicolet IS-10 FTIR model using KBr pellets over the wavenumber 4000-400 cm^{-1} for the synthesized materials.

2.4.2. X-ray diffraction (XRD)

The phase structures of the samples were investigated using XRD analysis. Patterns of the samples were analyzed at room temperature by X'Pert PRO PANalytical Corporation, Netherlands diffractometer with Cu Ka radiation in the 2θ range (5-80°). The average particle size (D) of the synthesized samples was calculated applying Scherer's equation (Eq. (1)).

$$\boldsymbol{D = \frac{K\lambda}{\beta\, Cos\, \theta}} \qquad \textbf{(1)}$$

Where: λ is the wavelength of Cu, K is α radiation, β is the full width at half maximum of the corresponding peaks, and β = FWHM. Π/180, K is considered unity, and θ is the position of the peak maximum.

2.4.3. Transmission Electron Microscopy (TEM) and Energy-dispersive X-ray (EDX)

TEM, Model JEM-200CX, JEOL 2100, Japan, operated at 200 kV equipped with EDX spectroscopy were operated to investigate the morphology and chemical composition of $NiFe_2O_4$-Mod MMT nanocomposite, respectively. A drop of the dispersed sample by ultrasonic treatment for 10 min was dripped on a TEM grid and dried prior to insertion to the TEM column.

2.4.4. Surface Zeta potential

The surface Zeta potential of the synthesized nanoadsorbent $NiFe_2O_4$-Mod MMT was characterized by the Zetasizer Nano (Malvern, UK), the pH of solution is ranged between 2 and 10, and temperature is 25 ℃.

2.4.5. Magnetic properties (VSM)

The evaluation of the magnetic properties of the nanoadsorbent was conducted using a vibrating sample magnetometer (VSM 7407, Lake Shore, USA) at a temperature of 25 ℃.

2.4.6. Surface area study

The specific surface area and pore size distribution of the nanoadsorbent were calculated by Brunauer-Emmett-Teller (BET) and Barrett-Joyner-Halanda (BJH) methods, respectively.

2.5. Adsorption study

The removal of Cu (II) and Zn (II) ions by ($NiFe_2O_4$-Mod MMT) magnetic nanocomposite was performed by the batch technique. After adsorption, the magnetic nanocomposite particles were collected magnetically and the concentration of the remaining metal ions was determined by the Inductively (ICP-OES) with Ultra Sonic Nebulizer (USN). This Nebulizer decreases the detection limit of the instrument by 10%. The ICP instrument is Perkin Elmer Optima 5300, USA. Five factors affecting the adsorption process including contact time, $NiFe_2O_4$-Mod MMT composite dosage, metal ion initial concentration, solution pH, and temperature were explored.

2.5.1. Effect of metal ion initial concentration

The adsorption of the metal ion with different concentrations (from 2 to 12 mg/L for Zn (II) and from 2 to 20 mg/L for Cu (II)) was examined by adding a specific adsorbent dose (0.1 g) to the same solution volume (50 mL) for a specific long contact time (120 min) at 298 K, a specific stirring rate of 125 rpm, and constant pH values of 6.0 and 3.9 for Cu (II) and Zn (II) ions, respectively. The reactions were made in 100 mL conical flasks on a vibromatic shaker (model number: 3015 RUMO).

The removal percentage of adsorbed metal ions was calculated from (Eq. (2)):

$$\boldsymbol{Removal}\ \% = \frac{C_0 - C_e}{C_0} \times 100 \qquad (2)$$

where C_0 is the metal ion initial concentration (mg/L), and C_e is the remaining metal ion concentration after treatment (mg/L). The adsorption capacity (q_e; mg/g) of the adsorbed Cu (II) and Zn (II) ions was calculated by Eq. (3).

$$q_e = (C_0 - C_e)\ \frac{V}{W} \qquad (3)$$

where V (L) is the utilized volume of metal ions solution and W (g) is the added amount of adsorbent. Many variables have been examined for each metal ion, which are: initial metal ion concentration, contact time, pH, temperature, and adsorbent dose effect.

2.5.2. Effect of contact time and Cu (II) and Zn (II) adsorption kinetics

The contact time which is necessary to reach the equilibrium state was investigated at the specified concentrations of (13 and 6 mg/L for Cu (II) and Zn (II) ions respectively) without any change of the pH at 298 K. After mixing the adsorbent dose (0.1 g) and the metal ion solutions (50 mL) in many conical flasks, the flasks were stirred at a constant rate (125 rpm) using a vibromatic shaker and the reaction is stopped after different time intervals (from 5 to 120 min) and the nanoadsorbent was separated magnetically.

Additionally, this research included the best-fit equations for linear and non-linear forms of the two widely used kinetic models, namely pseudo-first-order (P-F-O) and pseudo-second-order (P-S-O) equations to examine the adsorption mechanism.

The pseudo-first-order kinetic model is represented by Eq. 4 [18].

$$ln(q_e - q_t) = ln\, q_e - \left(\frac{k_1}{2.303}\right) t \qquad (4)$$

where k_1 is the pseudo-first-order rate constant (min^{-1}). q_e (mg/g) and q_t refer, respectively, to the amount of metal ions adsorbed at equilibrium and at a time (t; min).

The pseudo-second-order model is expressed by Eq. 5 [18].

$$\frac{t}{q_t} = \frac{1}{k_2\, q_e^2} + \frac{1}{q_e} t \qquad (5)$$

Where k_2 ($g.mg.min^{-1}$) is the pseudo-second-order rate constant of adsorption.

2.5.3. Effect of pH

The pH values of the metal ions' prepared solutions before adding the adsorbent dose were 5.1 and 2.2 for Cu (II) and Zn (II), respectively which were raised to 6.0 and 3.9 after adding the adsorbent. The effect of pH change on the $NiFe_2O_4$-Mod MMT sorption of Cu (II) and Zn (II) was studied in the range of 2 to 6 (after which the metal ions precipitate in the hydroxide forms).

2.5.4. Effect of adsorbent dose

Various doses of $NiFe_2O_4$-Mod MMT adsorbent (0.05, 0.1, 0.15, 0.2, and 0.25 g) were added to 50 mL of the metal ion solutions (with concentrations 6 mg/L and 13 mg/L for Zn (II) and Cu (II), respectively).

2.5.5. Adsorption isotherms

The equilibrium data obtained in this study were analyzed in terms of three isotherms; Langmuir (Eq. 6), Freundlich (Eq. 7), and Temkin (Eq. 8).

$$\frac{C_e}{q_e} = \frac{C_e}{Q_{max}} + \frac{1}{Q_{max} K_L} \qquad (6)$$

$$log\, q_e = log\, K_f + \frac{1}{n} log\, C_e \qquad (7)$$

$$q_e = \frac{RT}{b} ln(K_T) + \frac{RT}{b} ln(C_e) \qquad (8)$$

where q_e (mg/g) is the adsorption capacity at equilibrium, C_e is the metal ion concentration at equilibrium (mg/L), Q_{max} (mg/g) is the maximum monolayer adsorption capacity, K_L (L/mg) is the Langmuir constant, K_f (mg/g) is the Freundlich constant, n is the Freundlich exponent (empirical parameter, dimensionless), K_T (L/gm) is the Temkin isotherm equilibrium binding constant, b is the

Temkin isotherm constant, R is the universal gas constant (8.314 J/mol/K), as well as T, is the room temperature (298 K).

The basic characteristic of the Langmuir isotherm model is represented in terms of 'R_L' a dimensionless equilibrium parameter, described by Eq. 9.

$$\boldsymbol{R_L = \frac{1}{1+K_L C_0}} \qquad \textbf{(9)}$$

where C_o (mg/L); the amount of initial adsorbate and K_L (L/mg); is the Langmuir constant. The parameter R_L is considered to be a more accurate adsorption indicator. The value of R_L suggested whether the adsorption is irreversible (R_L = 0), favorable (0 < R_L < 1), linear (R_L = 1) or unfavorable (R_L > 1) [19].

2.5.6. Adsorption thermodynamics

The thermodynamic parameters for the adsorption reaction and the values of K_L (Langmuir constant; L/mg) at different temperatures (T; K) were processed according to Van't Hoff equation (Eq. 10) [20]:

$$\boldsymbol{ln\, K_L = \frac{-\Delta H^0}{RT} + \frac{\Delta S^0}{R}} \qquad \textbf{(10)}$$

where ΔHº (kJ/mol) and ΔSº (kJ/mol.K) are enthalpy and entropy changes, respectively, and R is the gas constant. Plotting ln K_L against 1/T gives a straight line with a slope and an intercept equal to ΔHº/R and ΔSº/R, respectively from which enthalpy and entropy changes can be calculated.

The Gibbs free energy (ΔGº; kJ/mol) of adsorption was calculated from the following relation:

$$\boldsymbol{\Delta G° = \Delta H° - T\Delta S°} \qquad \textbf{(11)}$$

2.6. Reproducibility study

The reproducibility study of the adsorbent is important in the industrial, practical, and economic points of view of heavy metals removal from wastewater. It's led to a decrease in the total cost of materials. To investigate the reproducibility study of the $NiFe_2O_4$-Mod MMT nanoadsorbent, the experiments were performed by dispersing 0.1 g of metal ion-loaded adsorbent collected by an external magnetic field into deionized water in 0.2 Mol/L HCl (pH=2) and stirring for 2 h at 25 ºC. This process is repeated for consecutive four cycles with the same adsorbent at the maximum adsorption operating parameters to examine the recovered adsorbent efficiency.

3. Results and discussion

3.1. Structural analysis

Various structural characterizations were performed for the natural montmorillonite (MMT) before and after its mechanochemical modification (Mod MMT) and for the nickel ferrite-modified montmorillonite $NiFe_2O_4$-Mod MMT nanocomposite before and after Cu (II) and Zn (II) ions adsorption.

3.1.1. FTIR spectroscopy

The FTIR spectra of the natural montmorillonite (MMT) before and after its mechanochemical modification (Mod MMT) and of the nickel ferrite-modified montmorillonite ($NiFe_2O_4$-Mod MMT) nanocomposite before and after Cu (II) and Zn (II) ions adsorption are displayed in Fig. 1a-e. For the natural MMT sample (Fig.1a), the broad and intense band centered at 1137 cm^{-1} is due to the stretching vibrations of Si-O bonds in the $(SiO)_4$−tetrahedral layers [21, 22]. The bands at 552 cm^{-1}, 811 cm^{-1}, and 863 cm^{-1} are assigned to the layered Al-O-Si, Si-O-Si networks vibrations, and deformation mode of Al-OH-Mg which are characteristics for MMT [23-27]. The aforementioned bands were also recorded in the FTIR spectrum of the Mod MMT sample but with some changes in their intensities and positions. Particularly, the Si-O vibration band of the MMT was shifted to 1103 cm^{-1} in the Mod MMT spectrum (Fig.1b) suggesting the occurrence of changes in the tetrahedral structural layers of MMT due to modification. Also, the mentioned other MMT bands were shifted to 530 and 798 cm^{-1} indicating the changes of the layered networks of Mod MMT than those of the MMT due to acid activation of MMT which may be resulted in the alterations in the absorption bands of the octahedral cations [25]. Decreasing the intensity of the MMT bands after its acidic modification reflects the octahedral cations leaching from the MMT structure, causing the loss of water band hydroxyl groups coordinated to them without affecting the MMT crystalline structure as stated by other researchers [28]. Also, decreasing the intensity of the bands at 1600 and 3600 cm^{-1} related to the -OH groups may be ascribed to the replacement of H_2O molecules by those H^+ after acid activation of MMT. Additionally, the bands observed at 471 cm^{-1} and 1030 cm^{-1} in the Mod MMT spectrum are assigned to the Si-O-Si networks vibrations and Si-O stretching mode [23, 24]. The two broad bands located at 3468 cm^{-1} and 1638 cm^{-1} in the spectrum of MMT, ascribed to the -OH elongation mode and -OH distortion of water, respectively [29, 30], were shifted to 3420 cm^{-1} and 1625 cm^{-1} in the Mod MMT spectrum. This may be

ascribed to that during the acid activation of clay, the protons penetrate the clay layers attacking the -OH groups causing the alterations in the adsorption bands attributed to the -OH vibration and octahedral cations. The same findings were reported by other authors [31]. For both samples MMT and Mod MMT, the band at 3619 cm^{-1} is due to the -OH stretching vibrations of the Al-OH and Si-OH groups of montmorillonite clay [32]. The presence of bands at 3620 cm^{-1} and 1625 cm^{-1} of clay the presence of hydroxyl linkage [33]. Moreover, the absorption bands appeared at 780-798 cm^{-1} and the band at about 920-958 cm^{-1} can indicate the possible interference of gibbsite and kaolinite impurities for the studied sample [34, 35].

For the composite sample (Fig. 1c), the wide absorption band at the area of (2800–3700 cm^{-1}) may be allocated to the O–H stretching vibration of H_2O absorbed by the sample and the surface Si-OH and Al-OH groups [36]. The absorption bands that appeared at 3420, 1625, and 3620 cm^{-1} in the IR spectrum of Mod MMT sample are variable after spinel co-precipitation. The -OH stretching vibration band at 3420 cm^{-1} is shifted to lower wavenumber i.e. 3403 cm^{-1} in the nanocomposite with very strong broadening suggests that hydrogen bonding may exist between spinel/clay and water molecules in addition to the formation of more silanol groups i.e. Si-OH and Al-OH [11, 37]. Also, disappearing the band at 3620 cm^{-1}, and decreasing the intensity of the band at 1625 cm^{-1}, and shifting to 1600 cm^{-1}, suggesting that the strong interaction between the nickel ferrite spinel and the negatively charged clay mineral surfaces restricted their vibrations (Fig. 1). The bands at ~ 1384 and 1472 cm^{-1} combined with antisymmetric NO_3-stretching vibration arising from remaining nitrate groups were used in the preparation of $NiFe_2O_4$ spinel [38]. The band intensity at 902 cm^{-1} for the Mod MMT is changed and shifted to 912 cm^{-1} after spinel co-precipitation on Mod MMT clay. This may be clarified based on the relation of this band by the increased degeneration of the SiO_4 tetrahedral structure elongation derived from polarity change in the metal-oxygen (M–O) bonds when linkage formed due to the interaction of silicon with other elements [39]. In addition to the above mentioned result, the appearance of a new band at about 857 cm^{-1} in $NiFe_2O_4$-Mod MMT composite related to Si-O-Si and OH deformation that related to Mg^{2+} and Al^{3+} confirming the occurrence of changes in the chemical environment [40]. The presence of the nickel ferrite accounted for the appearance of two bands in the FTIR spectrum of the spinel-clay nanocomposite. Therefore, the characteristic bands at 606 and 510 cm^{-1} were indicative of spinel ferrite materials and are due to the vibration of the metal-oxygen (M-O) bond at the tetrahedral and the octahedral sites [41]. Usually, these two bands are allocated to vibrate ions in the crystal lattices [42]. This means that uniformly distributed ferrite particles are present.

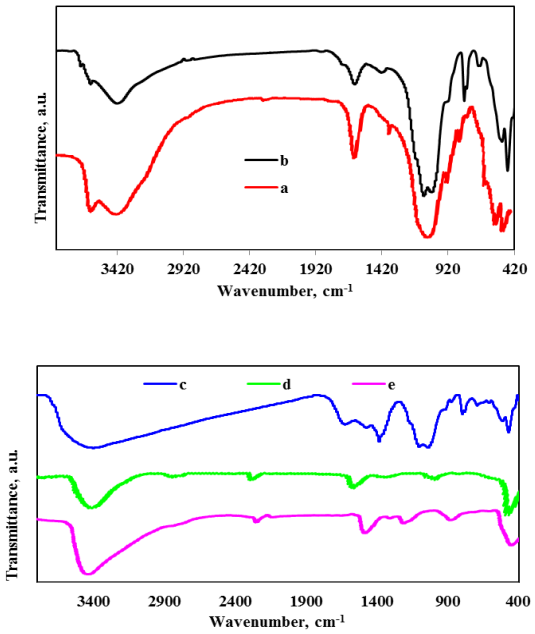

Fig. 1. FTIR of MMT (a), Mod MMT (b), $NiFe_2O_4$-Mod MMT nanocomposite before adsorption (c), and after adsorption of Cu (II) (d), and Zn (II) ions (e).

3.1.2. X-ray diffraction (XRD)

The XRD patterns of the natural MMT (MMT), modified MMT (Mod MMT), and that of nickel ferrite-modified montmorillonite ($NiFe_2O_4$-Mod MMT) nanocomposite before and after Cu (II) and Zn (II) ions adsorption are depicted in Fig. 2a-e. Several reflections characteristic for the montmorillonite crystalline structure at 2θ =7.23°, 19.8°, 26.73°, and 35.1° referred to the basal planes d001, d100, d103, and d006, respectively are observed in the XRD patterns of the natural MMT and Mod MMT samples (Fig.2a and b) [43, 44]. Also, the presence of the (080) diffraction peak at 2θ= 68.33° in their patterns reveals that montmorillonite has a dioctahedral structure [45]. The appearance of other reflections in their XRD patterns indicates the presence of impurities like quartz i.e., at 2θ = 26.7° [5] and kaolinite i.e., at 2θ of 20.9°, 35.1°, 36.6°, 39.5°, 42° and 45° [46]. There is no obvious change in the 2-theta values of the two samples indicating that the modification does not affect the crystalline structure of MMT. But the observed reduction in the intensities of the mentioned impurities reflections in the Mod MMT XRD patterns may be assigned to the octahedral cations leaching from the MMT structure [28, 47]. On the other hand,

the $NiFe_2O_4$-Mod MMT nanocomposite (Fig.2c) diffractogram demonstrates obvious changes in the XRD patterns relative to the Mod MMT sample which declares that the two compounds have efficiently interacted. The d001 peak of Mod MMT is shifted to a smaller angle i.e., 2θ of 4.33°, and becomes weak which may be correlated by the insertion of the $NiFe_2O_4$ spinel into the spaces between layers of the MMT clay [48, 49]. Additionally, decreasing the intensity of all reflections reveals the formation of an intercalated-MMT structure during the formation of the nanocomposite [22]. Moreover, two new peaks at 2θ = 29.43° and 34.78° have appeared that originate from $NiFe_2O_4$ spinel-type structure formation [50]. Bensalem et al. [51] reported that the movement of the d001 reflection for pure MMT to left side angle for CS/MMT bio-nanocomposites illustrates the achievement of an intercalated nanostructure, whereas the intensity decrease and peak broadening propose the existence of a jumbled intercalated or exfoliated structure. The average crystallite sizes (D) of (Pur-MMT) and $NiFe_2O_4$-Mod MMT samples are calculated by applying Scherer's formula. The average crystalline size is observed to be 24.39 nm and 15.74 nm for Mod MMT and $NiFe_2O_4$-Mod MMT composite, respectively revealed that the modified MMT and the synthesized composite are in the nano-scale. $NiFe_2O_4$-Mod MMT composite exhibited the lowest crystallite size in addition to the weakness of all reflections relative to Pur-MMT. This indicates the good dispersion of the deposited $NiFe_2O_4$ nanoparticles into the interlayer space of the intercalated MMT clay [52, 53].

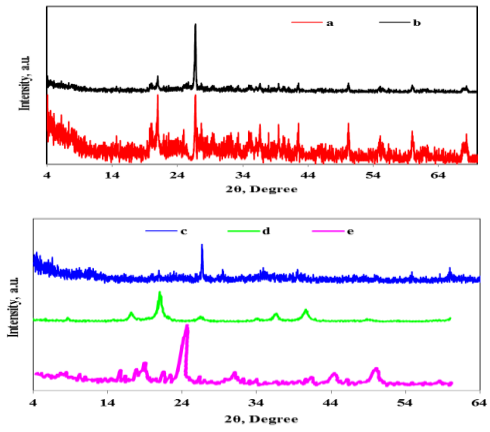

Fig. 2. XRD of MMT (a), Mod MMT (b), $NiFe_2O_4$-Mod MMT nanocomposite before adsorption (c), and after adsorption of Cu (II) (d), and Zn (II) ions (e).

3.1.3. Morphological analysis by TEM microscopy and EDX spectroscopy

Figures 3a and b show the TEM images of the freshly synthesized $NiFe_2O_4$-Mod MMT nanocomposite at different spots. TEM micrograph of the $NiFe_2O_4$-Mod MMT nanocomposite showed the existence of an intercalated structure of MMT as a result of MMT grinding [54, 55]. Although the ball milling modification could smash the particles of MMT clay [56], the intercalated MMT preserved the ''T–O–T'' structure according to the above observations [54, 57] which may be due to the lower time and power of milling. The TEM micrographs also revealed that the $NiFe_2O_4$ NPs (with an average size of 20 nm) of cubic morphology are uniformly packed with some agglomeration at the external surfaces of the Mod MMT clay matrix and near its edges as well as inserted into the interlayer spaces of the intercalated MMT clay [41, 58]. Thereby, TEM findings are in accordance with the discussed above results of FTIR and XRD.

For further confirmation, EDX spectroscopy was performed to define the chemical composition of the $NiFe_2O_4$-Mod MMT nanocomposite (Fig. 4 and Table 1). EDX results validate the existence of Ni, Fe, O, as well as Si and Al which represent all the synthesized $NiFe_2O_4$-Mod MMT nanocomposite elements confirming the homogeneous mixing of these elements in the nanocomposite and in accordance with the expected composition ratio.

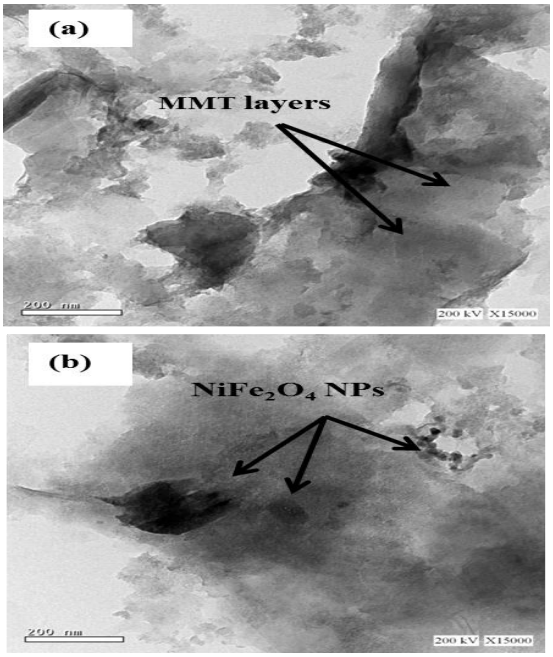

Fig. 3. (a and b)TEM images of $NiFe_2O_4$-Mod MMT nanocomposite at various spots.

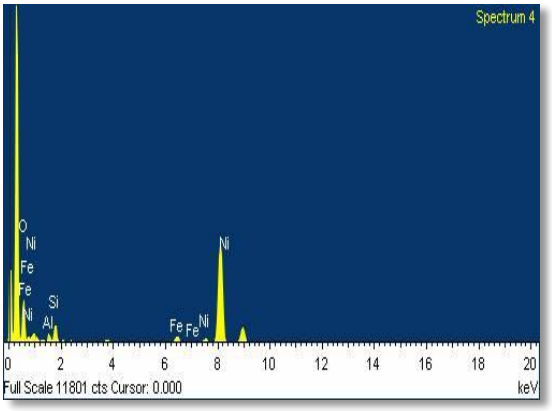

Fig. 4. EDX analysis of $NiFe_2O_4$-Mod MMT nanocomposite.

Table 1
Chemical composition of $NiFe_2O_4$-Mod MMT nanocomposite.

Element	Weight%	Atomic%
O K	38.86	63.51
Al K	5.14	4.98
Si K	12.50	11.64
Fe K	32.66	13.24
Ni K	10.84	6.63
Totals	**100.00**	

3.1.4. Magnetic properties(VSM)

The magnetic properties of the synthesized $NiFe_2O_4$-Mod MMT nanocomposite were studied by VSM analysis and the results are represented in the magnetization curve (Fig. 5). The saturation magnetization (emu/g) of $NiFe_2O_4$-Mod MMT nanocomposite was 74.54 emu/g confirming that this nanocomposite has a super paramagnetic behaviour [59] and its dispersed particles in water can be separated easily by an external magnetic field after adsorption equilibrium.

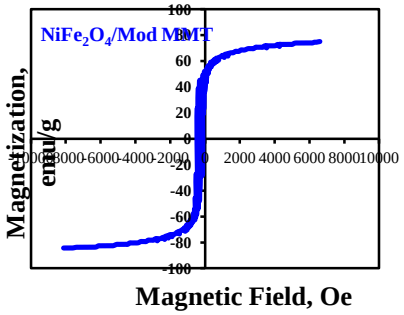

Fig. 5. VSM analysis of $NiFe_2O_4$-Mod MMT nanocomposite.

3.1.5. Surface area study

The adsorption-desorption isotherm of the synthesized $NiFe_2O_4$-Mod MMT nanocomposite is shown in Fig. 6 accompanied by an inset figure for the pore size distribution curve. The isotherm can be classified as type-IV according to IUPAC classification exhibiting H3 hysteresis loop, which is characteristic of non-uniform mesoporous texture [60]. This type indicates the presence of aggregates of plate-like particles giving rise to slit-shaped pores with nonuniform size and shape [61]. The pore size distribution curve confirms the presence of two sizes of pores; a defined peak appeared from 5.3 nm with a maximum centred at 8.71 nm, and a broader one centered at 12 nm. Additionally, the specific surface area results listed in Table 2 indicate that the total pore volume and the BET surface area of this composite are 0.186 (cm^3/g) and 114.77 (m^2/g), respectively. It's also showed that the nanoadsorbent average pore size (10.36 nm) are higher than the ionic sizes of Cu (II) (0.146 nm) and Zn (II) (0.148 nm) ions. So, it can be expected that the inner pores of the adsorbent may be involved in the adsorption of Cu (II) and Zn (II) ions but with higher adsorption removal for Cu (II) ions due to their smaller ionic size.

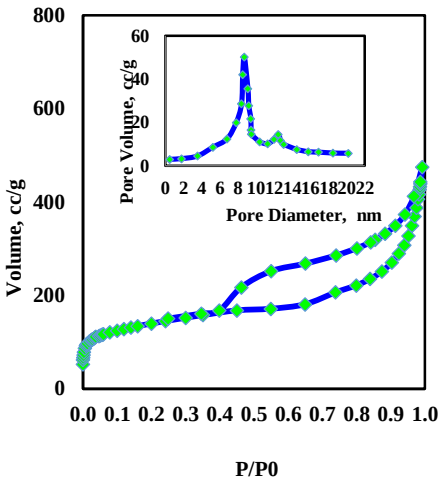

Fig. 6. N_2 adsorption-desorption isotherm of the synthesized $NiFe_2O_4$-Mod MMT nanocomposite and its pore size distribution (inset figure).

Table 2 Surface characteristics of the synthesized nanocomposite.

Sample	S_{BET}, m^2/g	Total pore volume, cm^3/g	Average pore diameter, nm
$NiFe_2O_4$/Mod MMT	114.77	0.186	10.36

3.1.6. Surface zeta potential

The zeta potential of $NiFe_2O_4$-Mod MMT nanoadsorbent at different PHs (2-12) is illustrated in Fig. 7. The point of zero charge (PZC) of this nanoadsorbent is at a pH of 4.7. At pHs greater than the pH_{PZC}, the surface charge of the nanoadsorbent is more negative which resulted in more cations adsorption capability [62]. It can be observed in Fig. 7 that the zeta potential is negative for almost the pH interval meaning that the surface charge of the nanoadsorbent is negative over a wide range of pH which increased its adsorption efficiency for the cations (Cu (II) and Zn (II) ions in this study).

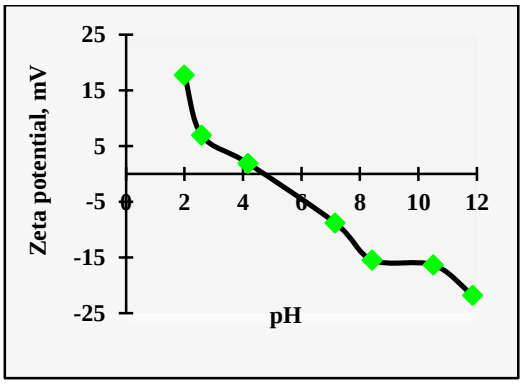

Fig. 7. Zeta potential of $NiFe_2O_4$-Mod MMT nanocomposite as a function of pH.

3.2. Adsorption studies

3.2.1. Effect of metal ion initial concentration

The initial concentration of metal ions has a very significant effect on the water treatment system; it specifies the maximum concentration with the higher removal percentage that can be treated by a specific amount of the adsorbent. Fig. 8 illustrates the relation between the initial metal ions' concentrations, in mg/L, and the corresponding removal percentage to each metal ion. For Cu (II) ions adsorption onto the $NiFe_2O_4$-Mod MMT magnetic adsorbent, the adsorption removal increases gradually with increasing the concentration from 2 mg/L to 13 mg/L, then decreases slightly with increasing the concentration from 13 mg/L to 20 mg/L. While for Zn (II) ions, the adsorption removal is constant with increasing the concentration from 2 mg/L to 4 mg/L, then decreases slightly with increasing the concentration from 4 mg/L to 12 mg/L. Due to the availability of a large number of the surface –OH and Si-O functional groups on $NiFe_2O_4$-Mod MMT nanoadsorbent for adsorption of Zn (II) and Cu (II) ions, the adsorption process was more efficient until it reaches the equilibrium concentration. After that, the removal percentage decreases because the extra ions have no available active sites to get adsorbed onto $NiFe_2O_4$-Mod MMT nanoadsorbent and the surface functional groups of the adsorbent were gradually saturated [63]. The equilibrium concentrations of Zn (II) and Cu (II) ions were 6 and 13 mg/L, respectively. The removal efficiencies were 91.67 and 99.23 % for Zn (II) and Cu (II) ions, respectively.

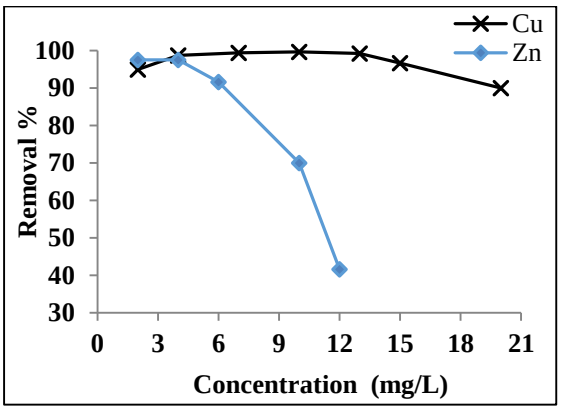

Fig. 8. Initial metal ions' concentrations versus removal% using $NiFe_2O_4$-Mod MMT nanocomposite.

3.2.2. Effect of contact time and Cu (II) and Zn (II) adsorption kinetics

The contact time impact on the adsorption process is presented in Fig. 9. The amount of metal ions adsorbed increased rapidly with time in the beginning, then non-linearly at a slower rate, and finally attained saturation called the equilibrium time (Fig. 9). As it is shown for Cu (II) metal ion, the equilibrium state was reached after 60 min of the reaction (the removal percentage was 99.23 %), while that for Zn (II) ions was reached after 90 min and the corresponding removal percentage was 91.67 %. After these two equilibrium states, the increase in the removal percentage is almost insignificant (less than 0.4 %). So, for the sake of saving time, times 60 and 90 min were considered the optimum ones for Cu (II) and Zn (II) ions respectively.

The results of pseudo-first-order (P-F-O) and pseudo-second-order (P-S-O) kinetic models are presented in Figs. 10a and b, respectively. The two models corresponding parameters (R^2, K, and q_e (mg/g) experimental and calculated metal ions uptake amounts) are illustrated in Table 3. The applicability of each model was examined by evaluating the correlation coefficient (R^2) and the matching between the experimental and calculated q_e (mg/g) values. Due to the higher R^2 values of pseudo-second-order for Zn (II) and Cu (II) ions adsorption onto $NiFe_2O_4$-Mod MMT adsorbent i.e. R^2 values are too close to unity (0.998 and 0.995 for Cu (II) and Zn (II) ions, respectively) and also the experimental and

calculated q_e (mg/g) values of P-S-O model are close to each other than those of the P-F-O model, the P-S-O model can be applied for the adsorption of Cu (II) and Zn (II) ions which means that the adsorption rate depends on chemical adsorption. This can be explained by the presence of –OH and Si-O surface functional groups on the $NiFe_2O_4$-Mod MMT magnetic adsorbent which are active in heavy metal ions binding [64, 65]. The P-F-O kinetic model can not be applied for the adsorption of Cu (II) and Zn (II) ions because the calculated q_e value for Cu (II) ion adsorption is much less than the experimental one.

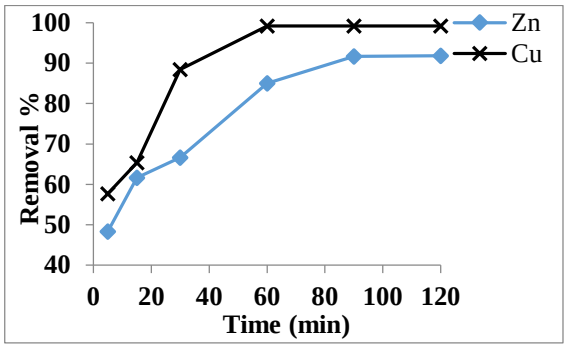

Fig. 9. Effect of contact time on the removal % of Cu (II) and Zn (II) ions.

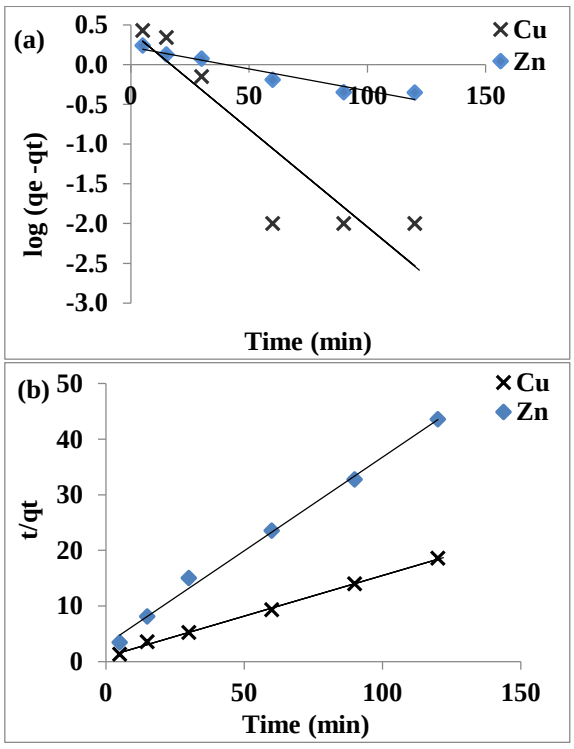

Figure 10: P-F-O model (a) and P-S-O model (b) application for Cu (II) and Zn (II) ions adsorption.

Table 3
Constants of the P-F-O and P-S-O models for Cu (II) and Zn (II) ions the adsorption.

Metal ion	Order	K (min^{-1})	Exp. q_e (mg/g)	Cal. q_e (mg/g)	R^2
Cu (II)	**P-F-O**	0.057	6.450	2.615	0.821
Cu (II)	**P-S-O**	0.026	6.450	6.821	0.998
Zn (II)	**P-F-O**	0.013	2.755	1.664	0.933
Zn (II)	**P-S-O**	0.037	2.755	2.966	0.995

3.2.3.Effect of pH

Metal sorption is critically bound to pH, each metal shows different ideal pH for its sorption. In general, adsorbents applied to heavy metal solutions usually induce a lowering of the pH, which is attributed to enhanced hydrolysis of the metals. It was found that the Cu (II) and Zn (II) ions uptake increases with the pH values increase as shown in Fig. 11. The optimum pH values were 5.0 and 6.0 for Cu (II) and Zn (II) ions, respectively. This can be attributed to that at a lower pH, the sorbent surface has a positive charge and electrostatic repulsion is formed between the $NiFe_2O_4$-Mod MMT adsorbent and the metal ions Cu (II) and Zn (II). Besides, the low adsorption of these metal ions at acidic pH may be because of the presence of excess smaller radius hydrogen ions (H^+) that compete with copper and zinc charges for the available surface sites of the sorbent [63, 66]. Thus by increasing the pH the opposite effect can be expected.

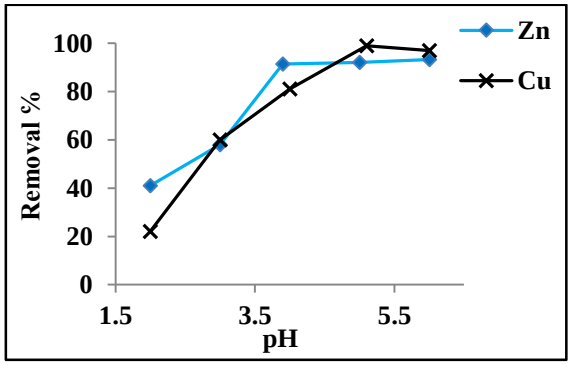

Fig. 11. pH versus removal % using $NiFe_2O_4$-Mod MMT nanocomposite.

3.2.4. Effect of adsorbent dose

The adsorptive release of Zn (II) and Cu (II) ions in relation to the $NiFe_2O_4$-Mod MMT adsorbent dose was shown in Fig. 12. The adsorption removal increases with raising the adsorbent dose, however, this increase was not very considerable. So, 0.1 g of the nanoadsorbent was considered as the optimum

dosage. The availability of more binding sites on the adsorbent surface and/or the larger surface area of $NiFe_2O_4$-Mod MMT nanocomposite for sorption may be the reason for the higher removal efficiency of the mentioned metal ions at high sorbent dosage [67, 68].

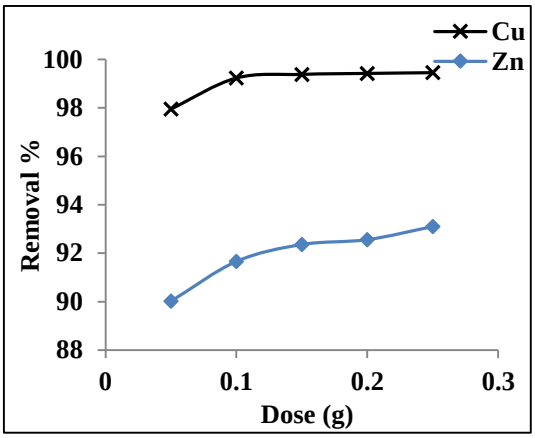

Fig. 12. Adsorbent dose versus removal (%) of Cu (II) and Zn (II) ions.

3.2.5. *Adsorption isotherms*

Three adsorption isotherms (Langmuir, Freundlich, and Temkin models) of Cu (II) and Zn (II) ions adsorption on $NiFe_2O_4$-Mod MMT nanocomposite are displayed in Figures 13-15. Also, Table 4 summarized the constants of the three isotherms estimated utilizing regression analysis of the experimental data.

3.2.5.1. *Langmuir isotherm*

Plotting the relation between C_e/q_e and C_e for the two metal ions produces a straight line (R^2 is too close to 1) that satisfies with a good agreement the Langmuir isotherm as shown in Fig. 13a and b. From the straight line slope and intercept, the Langmuir isotherm constants (Q_{max}, K_L, and R_L) are calculated (Table 4). Comparing the values of q_e (measured experimentally) and Q_{max} (calculated), it is clear that they are consistent with each other, which confirms the application of the equation meaning that the adsorption is monolayer and chemisorption [69].

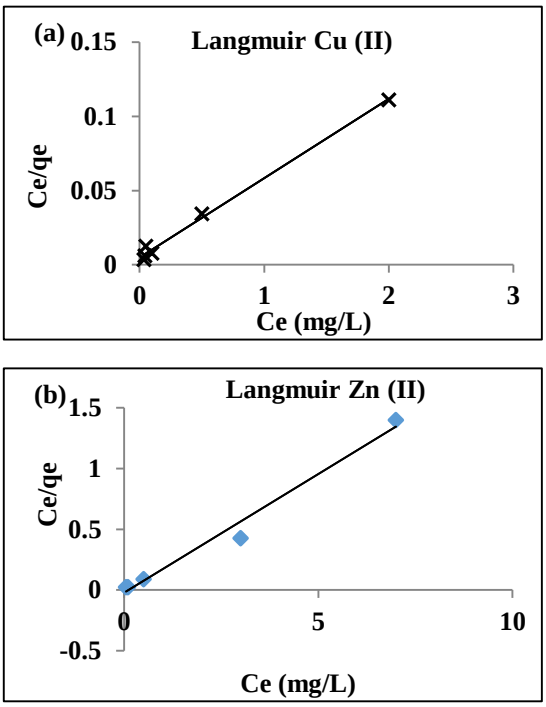

Fig. 13. Ce/qe versus Ce for Langmuir isotherm application of (a) Cu (II) and (b) Zn (II) adsorption

3.2.5.2. *Freundlich isotherm*

By drawing the relation between log C_e and log q_e (Fig. 14a and b), the Freundlich and exponent constants (K_f and n) are determined from the slope and intercept and of the straight lines. The estimated Freundlich isotherm constants and the related coefficients of correlation values are summarized in Table 4. The coefficient of correlation was low for the two metal ions (R^2 values are 0.549 and 0.613) indicating bad linearity. So, this model could not be applied in the case of using $NiFe_2O_4$-Mod MMT nanocomposite for Cu (II) and Zn (II) ions adsorption.

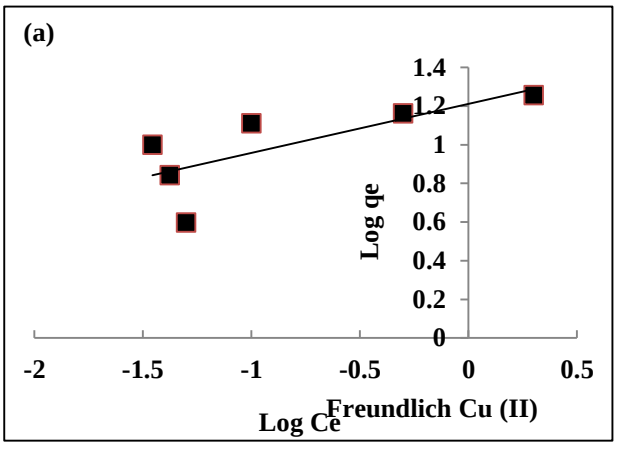

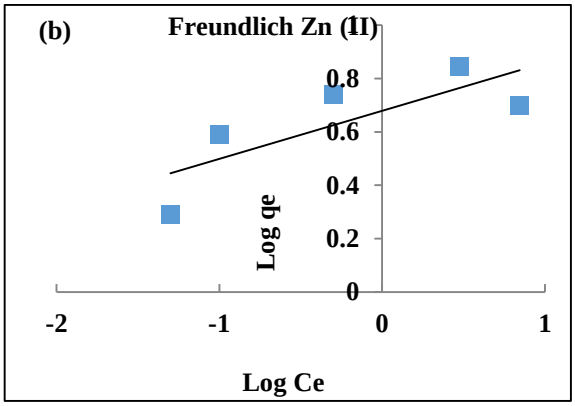

Fig. 14. Log(q_e) versus Log(C_e) for Freundlich isotherm application of (a) Cu (II) and (b) Zn (II) adsorption.

3.2.5.3. Temkin isotherm

By drawing the relation between log C_e and q_e (Fig. 15a and b), the Temkin isotherm equilibrium binding constant and the Temkin isotherm constant (A_T and b) are calculated from the intercept and slope of the straight line. The calculated Temkin constants and the corresponding coefficients of correlation values are summarized in Table 4. The coefficient of correlation was low for the two metal ions (R^2 values are 0.742 and 0.615 for Cu (II) and Zn (II), respectively indicating bad linearity. So, this model could not be applied in the case of using $NiFe_2O_4$-Mod MMT nanocomposite for the adsorption of the considered metal ions.

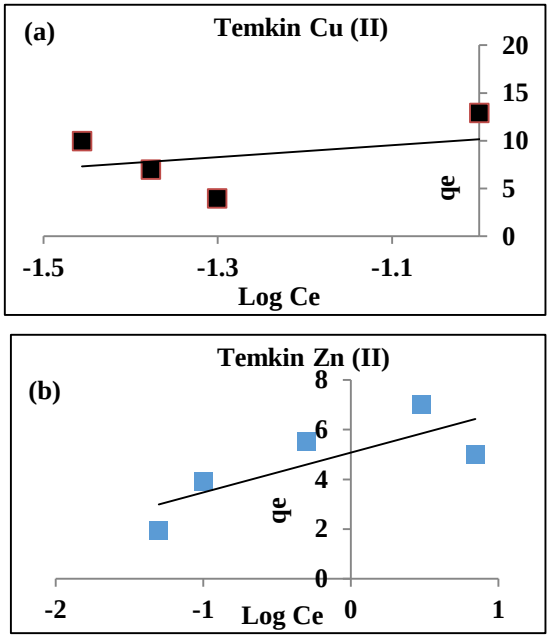

Fig. 15. q_e versus Log C_e for Temkin isotherm application of (a) Cu (II) and (b) Zn (II) adsorption.

Table 4
Constants of Langmuir, Freundlich, and Temkin isotherms for Cu (II) and Zn (II) ions adsorption.

Langmuir isotherm				
Metal ion	**Q_{max} (mg/g)**	**K_L (L/mg)**	**R_L**	**R^2**
Cu (II)	18.726	11.005	0.007	0.993
Zn (II)	5.128	9.213	0.018	0.983
Freundlich isotherm				
Metal ion	**n**	**K_f [(mg/g)/(mg/L)$^{1/n}$]**		**R^2**
Cu (II)	3.95	3.36		0.549
Zn (II)	5.54	1.97		0.613
Temkin isotherm				
Metal ion	**A_T (L/mg)**	**b_T (J/mol)**		**R^2**
Cu (II)	13.37	395.72		0.742
Zn (II)	23.75	487.62		0.615

From the mentioned three isotherms results, it can be concluded that the adsorption process of Cu (II) and Zn (II) ions on $NiFe_2O_4$-Mod MMT nanocomposite is well represented by the Langmuir isotherm model with a maximum monolayer adsorption capacity of 18.73 and 5.13 mg/g for Cu (II) and Zn (II) ions, respectively.

3.2.6. Effect of temperature and adsorption thermodynamics

The impact of temperature (298, 308, 318, and 328 K) on the removal percentages of considered metal ions Cu (II) and Zn (II) was investigated as shown in Fig. 16. It was found that the amount of adsorbed Cu (II) is independent of temperature, while the higher removal efficiency of Zn (II) is observed at higher temperatures. This is because at elevated temperatures, the kinetic energy of the adsorbate molecules increased which in turn increases the collision rate of the metal ion and the $NiFe_2O_4$-Mod MMT adsorbent. Moreover, it is well known that for the ions having the same valence, the smaller ion will hold hydration water more strongly resulting in weaker binding of the ion on the adsorbent. Herein, due to the smaller ionic radius of Cu (II) ion (0.073 nm) than that of Zn (II) ion (0.074 nm), the hydration layer of Cu (II) will hold strongly and the stability of the coordination bonds binding it with the adsorbent will get weaker and break easily at high temperature. Thus, the presence of difference in the obtained results for Cu (II) and Zn (II) ions adsorption at high temperatures is mainly influenced by their ionic radius.

Table 5 shows the thermodynamic parameters of the reaction. For both ions, the enthalpy change is

positive indicating that the reaction is endothermic, and the entropy change is positive too (less randomness), while ΔGº values are negative indicating that the process is spontaneous with a favorable sorption process [70].

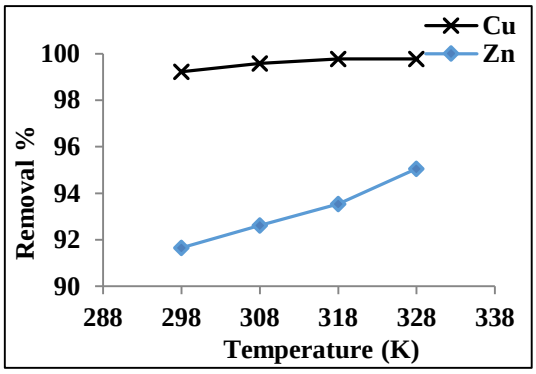

Fig. 16. Temperature (K) versus removal % using $NiFe_2O_4$-Mod MMT nanocomposite.

Table 5
Thermodynamic parameters for Cu (II) and Zn (II) ions the adsorption at various temperatures.

Parameter / Metal ion	T (K)	ΔS° (kJ/mol.K)	ΔH° (kJ/mol)	ΔG° (kJ/mol)
Cu (II)	298	124.4	24619.4	-12462.4
	308			-13706.8
	318			-14951.1
	328			-16195.5
Zn (II)	298	156.2	41271.5	-5274.6
	308			-6836.6
	318			-8398.5
	328			-9960.5

3.3. Adsorption Mechanism

To determine the adsorption mechanism of Cu (II) and Zn (II) ions onto $NiFe_2O_4$/Mod MMT nanoadsorbent, FTIR, and XRD analysis of the adsorbent before and after ions adsorption are displayed in Figs. 1 and 2 and discussed below.

3.3.1. FTIR spectrum for $NiFe_2O_4$/Mod MMT after ions adsorption

The FTIR spectrum of $NiFe_2O_4$/Mod MMT after Cu (II) and Zn (II) ions adsorption (Fig. 1d and e) indicates that the nanoadsorbent functional groups are slightly shifted from their positions and the intensity of the bands changed relative to the spectrum of this nanoadsorbent before ions adsorption (Fig. 1c). Typically, the wide FTIR band located at 2800-3700 cm^{-1} in the nanoadsorbent spectrum before ions adsorption due to the O–H groups of the surface Si-OH and Al-OH groups becomes less wide and shifted to 3467 cm^{-1} and 3500 cm^{-1} after the adsorption of Cu (II) and Zn (II) ions, respectively. The band located at 1600 cm^{-1} related to the -OH distortion of water is also shifted to 1597 cm^{-1} and 1517 cm^{-1} after the adsorption of Cu (II) and Zn (II) ions, respectively confirming the formation of a complex between the ions and water molecules present in MMT gallery [71]. The two bands appeared at 509 cm^{-1} (Fig.1d) and 483 cm^{-1} (Fig. 1e) in the spectrum of adsorbent after Cu (II) and Zn (II) ions are, respectively, assigned to Cu–O and Zn-O stretching vibrations. Moreover, the intensity and location of the Si-O vibrations of MMT tetrahedral layers that appeared in the fresh adsorbent at 1015 cm^{-1} and 1055 cm^{-1} were changed after ions adsorption indicating the binding of ions to the oxygen atoms present on the MMT surface as reported in [72]. The change in absorption intensity and the shift in wavenumber of functional groups could be attributed to the complexation between metal ions and binding sites (O of –OH group and O of Si-O groups) [73]. The oxygen of the –OH group has an available pair of electrons that can form coordinated covalent bonds with the metal cation. The aforementioned data show that the -OH and Si-O groups in the $NiFe_2O_4$/Mod MMT nanoadsorbent are involved in the ions adsorption process through the formation of a stable complex compound with Cu (II) and Zn (II) ions. Similar results were reported by other authors [74].

3.3.2. XRD pattern of $NiFe_2O_4$/Mod MMT after ions adsorption

The XRD pattern of $NiFe_2O_4$/Mod MMT after Cu (II) and Zn (II) ions adsorption are presented in Fig. 2d and e, respectively. These patterns present that the same reflection of the $NiFe_2O_4$/Mod MMT adsorbent is retained after ions adsorption with slight changes in the position and intensity of some peaks. These changes can be ascribed to ions' coordination with the oxygen of the –OH and Si-O groups that existed in the nanocomposite through the formation of a stable complex compound with Cu (II) and Zn (II) ions indicating that the precipitation reactions did not occur on the nanoadsorbent surface. This is in accordance with the FTIR results which indicate that the adsorption of Cu (II) and Zn (II) ions on the $NiFe_2O_4$/Mod MMT nanoadsorbent occurs mainly via surface complexation.

Based on the FTIR and XRD discussions mentioned above, the suggested mechanism for the adsorption of Cu (II) and Zn (II) ions onto $NiFe_2O_4$/Mod MMT magnetic nanoadsorbent is the surface complexation.

3.4. Reproducibility of the nanoadsorbent

The reproducibility results of $NiFe_2O_4$-Mod MMT magnetic nanoadsorbent toward sorption of Cu (II) and Zn (II) ions are displayed in Fig. 17. The results showed that after four cycles of Cu (II) or Zn (II) ions adsorption, removal efficiencies of 98.4% and 89.7% for Cu (II) and Zn (II) ions were provided for adsorbent reproducibility. These results showed a slight decrease in the efficiency of the adsorbent which can be ascribed to the loss of some active sites to the mentioned ions on the $NiFe_2O_4$-Mod MMT surface due to the ions' coordination with the surface functional groups after successive reproducibility cycles. Thus, $NiFe_2O_4$-Mod MMT magnetic nanoadsorbent could be a promising material for Cu (II) and Zn (II) ions adsorption from contaminated water.

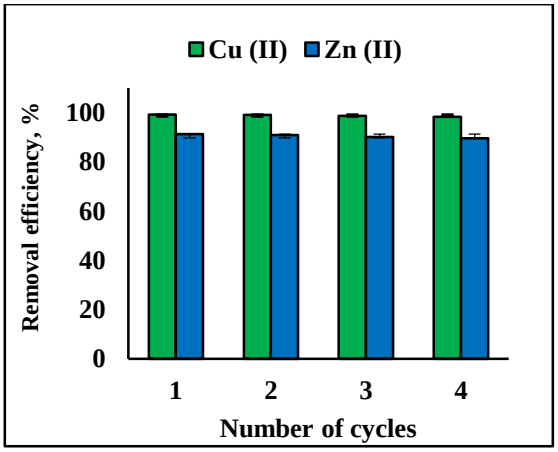

Fig. 17. The reproducibility results of $NiFe_2O_4$-Mod MMT magnetic nanoadsorbent toward sorption of Cu (II) and Zn (II) ions.

3.5. Competition with other elements

A mixed solution of different divalent metal ions (Cd (II), Pb (II), Ni (II), Cu (II), and Zn (II)) was prepared with a concentration of 5 mg/L for each metal ion. The adsorption tendency of the $NiFe_2O_4$-Mod MMT nanocomposite toward the considered ions was assessed in the presence of other ions as a competing factor by 50 mL of the prepared mixed solution and 0.1 g of the $NiFe_2O_4$-Mod MMT adsorbent dosage. The competitive adsorption results of Cu (II) and Zn (II) ions, in the mixture solution, are illustrated in Table 6. From the results, it is obvious that the $NiFe_2O_4$-Mod MMT nanocomposite has a high removal percentage (exceeding 90%) toward all the studied elements indicating the availability of surface functional groups as binding sites on the $NiFe_2O_4$-Mod MMT adsorbent surface for the sorption of the mentioned divalent heavy metals.

Table 6
Results of competitive experiments.

Metal ion	Concentration before treatment (mg/L)	Concentration after treatment (mg/L)	Removal (%)
Cd^{2+}	5	0.20	96
Pd^{2+}	5	0.43	91.4
Ni^{2+}	5	0.11	97.8
Cu^{2+}	5	0.19	96.2
Zn^{2+}	5	0.18	96.4

3.6. $NiFe_2O_4$/Mod MMT nanocomposite in comparison with other adsorbents

In this article, the use of a low-cost $NiFe_2O_4$/Mod MMT nanoadsorbent for the removal of Cu (II) and Zn (II) ions from polluted water was evaluated. Moreover, the magnetic properties of this nanocomposite represent an advantage for its separation at the end of the adsorption process.

Table 7 reviewed the maximum adsorption capacity (Q_{max}) of the $NiFe_2O_4$/Mod MMT nanocomposite towards Cu (II) and Zn (II) ions in comparison with some other adsorbents. The $NiFe_2O_4$/Mod MMT nanoadsorbent is superior in its adsorption capacity to most of these adsorbents for Cu (II) and Zn (II) ions removal due to the availability of a large number of oxygen-containing functional groups i.e. –OH and Si-O as binding sites on its surface for the sorption of these ions. Also, it still keeps about 98.4% and 89.7% of its removal efficiency after four consecutive cycles of reproducibility. More importantly, $NiFe_2O_4$/Mod MMT nanoadsorbent is a cost-effective adsorbent, and thanks to its magnetic properties it can be separated easily by an external magnetic field after adsorption equilibrium. Thus, it can be used as a potential alternative to today's expensive adsorbents for the elimination of Cu (II) and Zn (II) ions from polluted water.

Table 7
Maximum adsorption capacities of various adsorbents for Cu (II) and Zn (II) removal.

Adsorbent material	Q_{max} (mg/g)		Reference
	Cu (II)	Zn (II)	
Fe_3O_4 NPs	0.184	0.177	[75]
Fe_3O_4 .Bentonite	19.20	------	[76]
Fe_3O_4/MWCNTs	-----	3.759	[77]
Fe_3O_4-EC biochar	3.53	9.42	[78]
Chitosan immobilized on bentonite	14.9	----	[79]
Bentonite	18.43	----	[76]
chitosan/clay/magnetit	14.3	----	[80]
jatropha fruit wastes: biosorbents jatropha rind	11.54	14.85	[81]
$NiFe_2O_4$/Mod MMT	18.73	5.13	This Work

3.7. Cost analysis

Montmorillonite clay which is used in this study for $NiFe_2O_4$-Mod MMT nanocomposite synthesis is available naturally in the western desert of Egypt at no cost. However, the final product would cost approximately 200 L.E./Kg, that is, 12.77 USD/kg (~12693 USD/ton) including all expenses (clay transport, milling process, purification, electrical energy, and chemicals cost. Comparing the total cost of $NiFe_2O_4$-Mod MMT with the commercially available adsorbent (activated carbon), it is one and half times cheaper than activated carbon [82, 83]. Therefore, $NiFe_2O_4$-Mod MMT nanocomposite has an economic advantage over commercial activated carbon considering its valuable usage in Cu (II) and Zn (II) ions.

4. Conclusions

Nickel ferrite-mechanochemical modified montmorillonite nanocomposite as a new efficient cost-effective nanoadsorbent was successfully synthesized, characterized by various techniques, and utilized for the adsorption of Cu (II) and Zn (II) ions from polluted water. This study has found that maximum removal percentages of 99.23% and 91.67% of Cu (II) and Zn (II) ions respectively can be achieved by applying the eco-friendly synthesized $NiFe_2O_4$-Mod MMT nanoadsorbent. Batch experiments showed the varied effect on the adsorption cycle under-considered operating conditions. The adsorption process was well fitted by the pseudo-second-order kinetic model and the Langmuir isotherm model with a monolayer adsorption capacity of 18.73 and 5.13 mg/g for Cu (II) and Zn (II), respectively. Additionally, upon completion of the adsorption process in contaminated water, the magnetic properties of the synthesized nanocomposite represent an advantage for recovering its particles. Thus the current study suggests that $NiFe_2O_4$-Mod MMT magnetic nanocomposite can be used as an alternative to today's expensive adsorbents for the elimination of divalent heavy metals especially Cu (II) and Zn (II) ions from polluted water.

5. Conflicts of interest

There are no conflicts to declare.

6. Funding sources

This research received no specific grant from any funding agency in the public, commercial, or not-for-profit sectors.

7. Acknowledgments

The authors wish to express their sincere gratitude to the Egyptian Petroleum Research Institute (EPRI) and the National Water Research Center for providing all the possibilities for this research completion.

References

[1] N.K. Srivastava, C.B. Majumder, Novel biofiltration methods for the treatment of heavy metals from industrial wastewater, J Hazard Mater 151(1) (2008) 1-8.
[2] B. Ashish, K. Neeti, K. Himanshu, Copper toxicity: a comprehensive study, Research Journal of Recent Sciences 2277 (2013) 2502.
[3] O. Akpor, M. Muchie, Remediation of heavy metals in drinking water and wastewater treatment systems: Processes and applications, International Journal of Physical Sciences 5(12) (2010) 1807-1817.
[4] R. Petrus, J.K. Warchoł, Heavy metal removal by clinoptilolite. An equilibrium study in multi-component systems, Water Research 39(5) (2005) 819-830.
[5] A. Bée, L. Obeid, R. Mbolantenaina, M. Welschbillig, D. Talbot, Magnetic chitosan/clay beads: A magsorbent for the removal of cationic dye from water, Journal of Magnetism and Magnetic Materials 421 (2017) 59-64.
[6] R.-r. Shan, L.-g. Yan, K. Yang, S.-j. Yu, Y.-f. Hao, H.-q. Yu, B. Du, Magnetic Fe3O4/MgAl-LDH composite for effective removal of three red

dyes from aqueous solution, Chemical Engineering Journal 252 (2014) 38-46.
[7] Y. Yao, B. Gao, J. Fang, M. Zhang, H. Chen, Y. Zhou, A.E. Creamer, Y. Sun, L. Yang, Characterization and environmental applications of clay–biochar composites, Chem. Eng. J. 242 (2014) 136-143.
[8] L. Cornejo, R. Celis, C. Domínguez, M.C. Hermosín, J. Cornejo, Use of modified montmorillonites to reduce herbicide leaching in sports turf surfaces: Laboratory and field experiments, Appl Clay Sci 42(1-2) (2008) 284-291.
[9] A. Di Marsico, L. Scrano, M. Amato, B. Gàmiz, M. Real, L. Cox, Mucilage from seeds of chia (Salvia hispanica L.) used as soil conditioner; effects on the sorption-desorption of four herbicides in three different soils, Science of The Total Environment 625 (2018) 531-538.
[10] W. Zhang, L. Lu, Y. Cheng, N. Xu, L. Pan, Q. Lin, Y. Wang, Clean and rapid synthesis of double metal cyanide complexes using mechanochemistry, Green Chem. 13(10) (2011) 2701.
[11] S.M. Solyman, M.A. Betiha, The performance of chemically and physically modified local kaolinite in methanol dehydration to dimethyl ether, Egyptian Journal of Petroleum 23(3) (2014) 247-254.
[12] I. Tole, K. Habermehl-Cwirzen, A. Cwirzen, Mechanochemical activation of natural clay minerals: an alternative to produce sustainable cementitious binders – review, Mineralogy and Petrology 113(4) (2019) 449-462.
[13] V. Šepelák, D. Baabe, D. Mienert, D. Schultze, F. Krumeich, F. Litterst, K.D. Becker, Evolution of structure and magnetic properties with annealing temperature in nanoscale high-energy-milled nickel ferrite, Journal of Magnetism and Magnetic Materials 257(2-3) (2003) 377-386.
[14] L.P. Lingamdinne, Y.-L. Choi, I.-S. Kim, J.-K. Yang, J.R. Koduru, Y.-Y. Chang, Preparation and characterization of porous reduced graphene oxide based inverse spinel nickel ferrite nanocomposite for adsorption removal of radionuclides, Journal of hazardous materials 326 (2017) 145-156.
[15] M. Wawrzkiewicz, P. Bartczak, T. Jesionowski, Enhanced removal of hazardous dye form aqueous solutions and real textile wastewater using bifunctional chitin/lignin biosorbent, International journal of biological macromolecules 99 (2017) 754-764.
[16] V. Sinha, S. Chakma, Synthesis and evaluation of CMC-g-AMPS/Fe/Al/AC composite hydrogel and their use in fluoride removal from aqueous solution, Environmental Technology & Innovation 17 (2020) 100620.
[17] D. Saravanan, T. Gomathi, P. Sudha, Sorption studies on heavy metal removal using chitin/bentonite biocomposite, International journal of biological macromolecules 53 (2013) 67-71.
[18] J. Lin, L. Wang, Comparison between linear and non-linear forms of pseudo-first-order and pseudo-second-order adsorption kinetic models for the removal of methylene blue by activated carbon, Frontiers Environ Sci Eng 3(3) (2009) 320-324.
[19] W. Zhan, C. Xu, G. Qian, G. Huang, X. Tang, B. Lin, Adsorption of Cu (ii), Zn (ii), and Pb (ii) from aqueous single and binary metal solutions by regenerated cellulose and sodium alginate chemically modified with polyethyleneimine, RSC advances 8(33) (2018) 18723-18733.
[20] N.O. Tapabashi, A.N. Bahjat, F.M. Al-abady, Study of Thermodynamic and Kinetic Adsorption of Azo Dyes on Different Adsorbent Surfaces, Kirkuk University Journal for Scientific Studies 14(2) (2019) 273-296.
[21] A. Dos Santos, M. Viante, D. Pochapski, A. Downs, C. Almeida, Enhanced removal of p-nitrophenol from aqueous media by montmorillonite clay modified with a cationic surfactant, Journal of hazardous materials 355 (2018) 136-144.
[22] H. Yan, X. Chen, Y. Feng, F. Xiang, J. Li, Z. Shi, X. Wang, Q. Lin, Modification of montmorillonite by ball-milling method for immobilization and delivery of acetamiprid based on alginate/exfoliated montmorillonite nanocomposite, Polymer Bulletin 73(4) (2016) 1185-1206.
[23] M.A. Djebbi, S. Boubakri, Z. Bouaziz, M.S. Elayachi, P. Namour, N. Jaffrezic-Renault, A.B.H. Amara, Extended-release of chlorpromazine intercalated into montmorillonite clays, Microporous and Mesoporous Materials 267 (2018) 43-52.
[24] A. Moslemizadeh, S.K.-y. Aghdam, K. Shahbazi, H.K.-y. Aghdam, F. Alboghobeish, Assessment of swelling inhibitive effect of CTAB adsorption on montmorillonite in aqueous phase, Applied Clay Science 127 (2016) 111-122.
[25] F. Adzmi, S. Meon, M.H. Musa, N.A. Yusuf, Preparation, characterisation and viability of encapsulatedTrichoderma harzianumUPM40 in alginate-montmorillonite clay, J. Microencapsul. 29(3) (2012) 205-210.
[26] M.A. Djebbi, S. Boubakri, Z. Bouaziz, M.S. Elayachi, P. Namour, N. Jaffrezic-Renault, A. Ben Haj Amara, Corrigendum to: “Extended-release of chlorpromazine intercalated into montmorillonite clays” [Microporous and Mesoporous Materials 267 (2018) 43–52],

Microporous and Mesoporous Materials 284 (2019) 486.
[27] A. Moslemizadeh, S. Khezerloo-ye Aghdam, K. Shahbazi, H. Khezerloo-ye Aghdam, F. Alboghobeish, Assessment of swelling inhibitive effect of CTAB adsorption on montmorillonite in aqueous phase, Applied Clay Science 127-128 (2016) 111-122.
[28] S. Bendou, M. Amrani, Effect of Hydrochloric Acid on the Structural of Sodic-Bentonite Clay, Journal of Minerals and Materials Characterization and Engineering 02(05) (2014) 404-413.
[29] A. Bartolozzi, R. Bertani, E. Burigo, A. Fabrizi, F. Panozzo, M. Quaresimin, F. Simionato, P. Sgarbossa, S. Tamburini, M. Zappalorto, Multifunctional Cu2+-montmorillonite/epoxy resin nanocomposites with antibacterial activity, Journal of Applied Polymer Science 134(16) (2017).
[30] G. Lv, Z. Li, W.-T. Jiang, P.-H. Chang, L. Liao, Interlayer configuration of ionic liquids in a Ca-montmorillonite as evidenced by FTIR, TG-DTG, and XRD analyses, Materials Chemistry and Physics 162 (2015) 417-424.
[31] A.S. Özcan, B. Erdem, A. Özcan, Adsorption of Acid Blue 193 from aqueous solutions onto BTMA-bentonite, Colloids and Surfaces A: Physicochemical and Engineering Aspects 266(1-3) (2005) 73-81.
[32] E.K. Putra, R. Pranowo, J. Sunarso, N. Indraswati, S. Ismadji, Performance of activated carbon and bentonite for adsorption of amoxicillin from wastewater: Mechanisms, isotherms and kinetics, Water research 43(9) (2009) 2419-2430.
[33] H.W. Van der Marel, H. Beutelspacher, Atlas of infrared spectroscopy of clay minerals and their admixtures, Elsevier Publishing Company.1976.
[34] E.W. Maina, H.J. Wanyika, A.N. Gacanja, Instrumental Characterization of Montmorillonite Clay by FT-IR and XRD from J.K.U.A.T Farm, in the Republic of Kenya, Chemistry and Materials Research 7(10) (2015) 43:49.
[35] B.J. Saikia, G. Parthasarathy, Fourier transform infrared spectroscopic characterization of kaolinite from Assam and Meghalaya, Northeastern India, Journal of Modern Physics 1(04) (2010) 206.
[36] P. Sivakumar, R. Ramesh, A. Ramanand, S. Ponnusamy, C. Muthamizhchelvan, Synthesis and characterization of nickel ferrite magnetic nanoparticles, Materials Research Bulletin 46(12) (2011) 2208-2211.
[37] X. Yan, L. Zhang, Y. Zhang, G. Yang, Z. Yan, Amine-modified SBA-15: effect of pore structure on the performance for CO2 capture, Industrial & Engineering Chemistry Research 50(6) (2011) 3220-3226.
[38] J. Xiang, X. Shen, F. Song, M. Liu, One-dimensional NiCuZn ferrite nanostructures: Fabrication, structure, and magnetic properties, Journal of Solid State Chemistry 183(6) (2010) 1239-1244.
[39] B.L. Newalkar, J. Olanrewaju, S. Komarneni, Direct synthesis of titanium-substituted mesoporous SBA-15 molecular sieve under microwave− hydrothermal conditions, Chemistry of Materials 13(2) (2001) 552-557.
[40] B. Wang, H. Ding, Y. Deng, Characterization of calcined kaolin/TiO 2 composite particle material prepared by mechano-chemical method, Journal of Wuhan University of Technology-Mater. Sci. Ed. 25(5) (2010) 765-769.
[41] M.K. Lima-Tenório, L.A.S. Oliveira, M.R. Guilherme, E.T. Tenório-Neto, M.F. Silva, D.M. Fernandes, A.A.W. Hechenleitner, E.A.G. Pineda, Tuning the magnetic properties of ferrite nanoparticles by Zn and Co doping, Materials Letters 195 (2017) 151-155.
[42] P. Sivakumar, R. Rameshb, A. Ramanand, S. Ponnusamy, C. Muthamizhchelvan, Synthesis, studies and growth mechanism of ferromagnetic $NiFe_2O_4$ nanosheet, Applied Surface Science 258 (2012) 6648:6652.
[43] A.S.K. Kumar, S. Kalidhasan, V. Rajesh, N. Rajesh, A meticulous study on the adsorption of mercury as tetrachloromercurate (II) anion with trioctylamine modified sodium montmorillonite and its application to a coal fly ash sample, Industrial & Engineering Chemistry Research 51(35) (2012) 11312-11327.
[44] N. Sarier, E. Onder, S. Ersoy, The modification of Na-montmorillonite by salts of fatty acids: An easy intercalation process, Colloids and Surfaces A: Physicochemical and Engineering Aspects 371(1-3) (2010) 40-49.
[45] J. Hu, X. Tan, X. Ren, X. Wang, Effect of humic acid on nickel(ii) sorption to Ca-montmorillonite by batch and EXAFS techniques study, Dalton Transactions 41(35) (2012) 10803.
[46] E. Maina, H. Wanyika, A. Gacanja, Natural Pyrethrum Extracts Photo-stabilized with Organo Clays, Journal of Scientific Research and Reports 9(7) (2016) 1-20.
[47] S.K. Bharadwaj, P.K. Boruah, P.K. Gogoi, Phosphoric acid modified montmorillonite clay: A new heterogeneous catalyst for nitration of arenes, Catalysis Communications 57 (2014) 124-128.
[48] A. dos Santos, M.F. Viante, D.J. Pochapski, A.J. Downs, C.A.P. Almeida, Enhanced removal of p-nitrophenol from aqueous media by montmorillonite clay modified with a cationic surfactant, Journal of Hazardous Materials 355 (2018) 136-144.
[49] H.A. Youssef, Z.I. Ali, K.F. El-Nemr, M. Bekhit, Effect of ionizing radiation on the

properties of acrylonitrile butadiene rubber/clay nanocomposites, Journal of Elastomers & Plastics 45(5) (2012) 407-428.
[50] Mohammed H, Abdul Latif, F.L. Yahya, Preparation and Characterization of New Magnetic Montmorillonite Clay Mineral by Intercalation of Iron Oxides in West Iraqi Layered Bentonite Chemistry and Materials Research 7(8) (2015) 55:62.
[51] S. Bensalem, B. Hamdi, S. Del Confetto, M. Iguer-Ouada, A. Chamayou, H. Balard, R. Calvet, Characterization of chitosan/montmorillonite bionanocomposites by inverse gas chromatography, Colloids and Surfaces A: Physicochemical and Engineering Aspects 516 (2017) 336-344.
[52] D. Jnaneshwara, D. Avadhani, B.D. Prasad, B. Nagabhushana, H. Nagabhushana, S. Sharma, C. Shivakumara, J. Rao, N. Gopal, S.-C. Ke, Electron paramagnetic resonance, magnetic and electrical properties of CoFe2O4 nanoparticles, Journal of Magnetism and Magnetic Materials 339 (2013) 40-45.
[53] M.K. Lima-Tenório, L.A. Oliveira, M.R. Guilherme, E.T. Tenório-Neto, M.F. Silva, D.M. Fernandes, A.A. Hechenleitner, E.A. Pineda, Tuning the magnetic properties of ferrite nanoparticles by Zn and Co doping, Materials Letters 195 (2017) 151-155.
[54] H. Yan, X. Chen, Y. Feng, F. Xiang, J. Li, Z. Shi, X. Wang, Q. Lin, Modification of montmorillonite by ball-milling method for immobilization and delivery of acetamiprid based on alginate/exfoliated montmorillonite nanocomposite, Polymer Bulletin 73(4) (2015) 1185-1206.
[55] X. Yan, L. Zhang, Y. Zhang, G. Yang, Z. Yan, Amine-Modified SBA-15: Effect of Pore Structure on the Performance for CO2Capture, Ind. Eng. Chem. Res. 50(6) (2011) 3220-3226.
[56] M. Gao, P.-x. Zhu, A starch/milled-montmorillonite nanocomposite for warp sizing, Starch - Stärke 64(2) (2011) 97-104.
[57] Y. Chenglin, Y. Yiqun, Z. Ye, L. Na, L. Xiaoya, L. Jing, J. Ming, Self-Assembly and Emulsification of Poly{[styrene-alt-maleic acid]-co-[styrene-alt-(N-3,4-dihydroxyphenylethyl-maleamic acid)]}, Langmuir 28(25) (2012) 9211-9222.
[58] A.B. Bourlinos, E. Devlin, N. Boukos, A. Simopoulos, D. Petridis, Magnetite and Co ferrite-based clay composites, Clay Minerals 37(1) (2002) 135-141.
[59] M.A. Dheyab, A.A. Aziz, M.S. Jameel, O.A. Noqta, P.M. Khaniabadi, B. Mehrdel, Simple rapid stabilization method through citric acid modification for magnetite nanoparticles, Sci. Rep. 10(1) (2020).
[60] K.S.W. Sing, Reporting physisorption data for gas/solid systems with special reference to the determination of surface area and porosity (Recommendations 1984), Pure Appl. Chem. 57(4) (1985) 603-619.
[61] A. Lecloux, J.P. Pirard, The importance of standard isotherms in the analysis of adsorption isotherms for determining the porous texture of solids, J. Colloid Interface Sci. 70(2) (1979) 265-281.
[62] S. Lin, Heavy metal removal from water by sorption using surfactant-modified montmorillonite, Journal of Hazardous Materials 92(3) (2002) 315-326.
[63] S. Guo, P. Jiao, Z. Dan, N. Duan, G. Chen, J. Zhang, Preparation of L-arginine modified magnetic adsorbent by one-step method for removal of Zn (Ⅱ) and Cd (Ⅱ) from aqueous solution, Chemical engineering journal 317 (2017) 999-1011.
[64] A. Dolgormaa, C.-j. Lv, Y. Li, J. Yang, J.-x. Yang, P. Chen, H.-p. Wang, J. Huang, Adsorption of Cu (II) and Zn (II) ions from aqueous solution by gel/PVA-modified super-paramagnetic iron oxide nanoparticles, Molecules 23(11) (2018) 2982.
[65] N.N. Dil, M. Sadeghi, Free radical synthesis of nanosilver/gelatin-poly (acrylic acid) nanocomposite hydrogels employed for antibacterial activity and removal of Cu (II) metal ions, Journal of hazardous materials 351 (2018) 38-53.
[66] Y. Ren, X. Wei, M. Zhang, Adsorption character for removal Cu (II) by magnetic Cu (II) ion imprinted composite adsorbent, Journal of hazardous materials 158(1) (2008) 14-22.
[67] Y. Dai, K. Zhang, J. Li, Y. Jiang, Y. Chen, S. Tanaka, Adsorption of copper and zinc onto carbon material in an aqueous solution oxidized by ammonium peroxydisulphate, Separation and Purification Technology 186 (2017) 255-263.
[68] F.A. Dawodu, K.G. Akpomie, Simultaneous adsorption of Ni(II) and Mn(II) ions from aqueous solution unto a Nigerian kaolinite clay, Journal of Materials Research and Technology 3(2) (2014) 129-141.
[69] Y. Zhang, L. Bai, W. Zhou, R. Lu, H. Gao, S. Zhang, Superior adsorption capacity of Fe3O4@ nSiO2@ mSiO2 core-shell microspheres for removal of congo red from aqueous solution, Journal of Molecular Liquids 219 (2016) 88-94.
[70] J. Lacey, Cross Section Measurements of the Higgs Boson in the Diphoton Decay Channel Using Proton-Proton Collision Data Recorded by

the ATLAS Detector at Centre-of-Mass Energies of 7 TeV and 8 TeV, Carleton University.
[71] H. Medhi, K.G. Bhattacharyya, Retracted Article: Kinetic and mechanistic studies on adsorption of Cu(ii) in aqueous medium onto montmorillonite K10 and its modified derivative, New Journal of Chemistry 41(22) (2017) 13533-13552.
[72] Z. Ibrahim, B. Koubaissy, Y. Mohsen, T. Hamieh, T.J. Daou, H. Nouali, M.-L. Foddis, J. Toufaily, Adsorption of Pyridine onto Activated Montmorillonite Clays: Effect Factors, Adsorption Behavior and Mechanism Study, American Journal of Analytical Chemistry 09(10) (2018) 464-481.
[73] S.N.M. Yusoff, A. Kamari, W.P. Putra, C.F. Ishak, A. Mohamed, N. Hashim, I.M. Isa, Removal of Cu(II), Pb(II) and Zn(II) Ions from Aqueous Solutions Using Selected Agricultural Wastes: Adsorption and Characterisation Studies, J. Environ. Prot. (Irvine, Calif.) 05(04) (2014) 289-300.
[74] X. Yu, S. Tong, M. Ge, L. Wu, J. Zuo, C. Cao, W. Song, Adsorption of heavy metal ions from aqueous solution by carboxylated cellulose nanocrystals, Journal of Environmental Sciences 25(5) (2013) 933-943.
[75] L. Giraldo, A. Erto, J.C. Moreno-Piraján, Magnetite nanoparticles for removal of heavy metals from aqueous solutions: synthesis and characterization, Adsorption 19(2) (2013) 465-474.
[76] L. Yan, S. Li, H. Yu, R. Shan, B. Du, T. Liu, Facile solvothermal synthesis of Fe3O4/bentonite for efficient removal of heavy metals from aqueous solution, Powder Technology 301 (2016) 632-640.
[77] L. Jiang, S. Li, H. Yu, Z. Zou, X. Hou, F. Shen, C. Li, X. Yao, Amino and thiol modified magnetic multi-walled carbon nanotubes for the simultaneous removal of lead, zinc, and phenol from aqueous solutions, Applied Surface Science 369 (2016) 398-413.
[78] B.C. Nyamunda, T. Chivhanga, U. Guyo, F. Chigondo, Removal of Zn (II) and Cu (II) ions from industrial wastewaters using magnetic biochar derived from water hyacinth, Journal of Engineering 2019 (2019).
[79] M.K. Thakur, V.K. Thakur, R.K. Gupta, A. Pappu, Synthesis and applications of biodegradable soy based graft copolymers: a review, ACS Sustainable Chemistry & Engineering 4(1) (2016) 1-17.
[80] D.-W. Cho, B.-H. Jeon, C.-M. Chon, Y. Kim, F.W. Schwartz, E.-S. Lee, H. Song, A novel chitosan/clay/magnetite composite for adsorption of Cu (II) and As (V), Chemical Engineering Journal 200 (2012) 654-662.
[81] H. Nacke, A.C. Gonçalves, M.A. Campagnolo, G.F. Coelho, D. Schwantes, M.G. dos Santos, D.L. Briesch, J. Zimmermann, Adsorption of Cu (II) and Zn (II) from Water by Jatropha curcas L. as Biosorbent, Open Chemistry 14(1) (2016) 103-117.
[82] L. Giraldo, A. Erto, J.C. Moreno-Piraján, Magnetite nanoparticles for removal of heavy metals from aqueous solutions: synthesis and characterization, Adsorption 19(2-4) (2013) 465-474.
[83] T. Wen, J. Wang, X. Li, S. Huang, Z. Chen, S. Wang, T. Hayat, A. Alsaedi, X. Wang, Production of a generic magnetic Fe3O4 nanoparticles decorated tea waste composites for highly efficient sorption of Cu(II) and Zn(II), Journal of Environmental Chemical Engineering 5(4) (2017) 3656-3666.